Asian Journal of Pharmaceutical Sciences 20 (2025) 100992

Available online at www.sciencedirect.com

ScienceDirect

journal homepage: www.elsevier.com/locate/AJPS

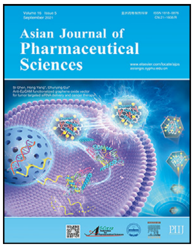

Research Article

Tailoring carrier-free nanoparticles based on natural small molecule assembly for synergistic anti-tumor efficacy

Di Wu[a,c], *Bin Zhou*[b], *Ying Liu*[d], *Xiao Zhu*[e], *Bin Li*[a], *Hongshan Liang*[a,*]

[a] *College of Food Science and Technology, Huazhong Agricultural University, Wuhan 430070, China*

[b] *Key Laboratory of Fermentation Engineering, Ministry of Education, National "111" Center for Cellular Regulation and Molecular Pharmaceutics, Hubei Key Laboratory of Industrial Microbiology, School of Biological Engineering and Food, Hubei University of Technology, Wuhan 430068, China*

[c] *College of Food Science and Engineering, Qingdao Agricultural University, Qingdao 266109, China*

[d] *Department of Gynecology, Qingdao Hiser Hospital Affiliated of Qingdao University (Qingdao Traditional Chinese Medicine Hospital), Qingdao, 266033, China*

[e] *Research Computing, Purdue University, West Lafayette IN 47905, USA*

ARTICLE INFO

Article history:
Received 29 May 2024
Revised 23 August 2024
Accepted 25 September 2024
Available online 8 November 2024

Keywords:
Tannic acid
Oxidative self-polymerization
Nanoparticles
Drug delivery
Anti-tumor

ABSTRACT

Interfacial modular assemblies of versatile polyphenols have attracted widespread interest in surface and materials engineering. In this study, natural polyphenol (tannic acid, TA) and nobiletin (NOB) can directly form binary carrier-free spherical nanoparticles (NT NPs) through synergistically driven by a variety of interactions (such as hydrogen bonding, oxidative reactions, etc.). The synthesis involves polyphenolic deposition on hydrophobic NOB nanoaggregates, followed by *in situ* oxidative self-polymerization. Interestingly, the assembled NT NPs exhibit controllable and dynamic changes in particle size during the initial stage. Ultimately, uniform and spherical NT NPs appear stable, with high loading capability, enabling incorporated NOB to preserve their function. Furthermore, *in vitro* evaluations demonstrate that the rational combination of polyphenol module and NOB can induce apoptosis and inhibit tumor metastasis for both lung cancer H1299 and human fibrosarcoma HT1080 cell lines. Notably, the optimized NT48 NPs were then verified *in vivo* experiments to achieve a promising synergistic anti-tumor efficacy. These findings not only provide new opportunities for the streamlined and sensible engineering of future polyphenol-based biomaterials, but also open up new prospects for the design of small-molecule nature phytochemicals.

---

* Corresponding author.
E-mail address: lianghongshan@mail.hzau.edu.cn (H. Liang).

Peer review under responsibility of Shenyang Pharmaceutical University.

https://doi.org/10.1016/j.ajps.2024.100992

1. Introduction

Polyphenols, due to their unique structural properties (*e.g.*, catechol or pyrogallol units) [1], have long been considered ideal precursors in materials engineering [2,3]. Indeed, plant polyphenols have received broad attention because of their ability to deposit onto various substrate surfaces spontaneously [4–7]. The deposition occurs preliminarily due to the strong interfacial bonding between polyphenols and substrate surfaces. It is noteworthy that polyphenols are prone to be embedded in specific ligands (such as proteins [7,8], small molecule compounds [9,10], and multivalent metal ions [11,12]), which further facilitates the deposition process. For example, Polyphenols interacting with PEG or proteins through hydrogen bonding are capable of promoting deposition [13,14]. The coordination interaction occurs between TA and metal ions can facilitate the deposition process as well [11]. In the design of molecular building blocks for anchoring surface decoration, the construction of polyphenol-containing assembly is being extensively investigated for several applications, including biosensing, catalysis, drug delivery, etc.

Recently, efforts have been focused on polyphenol-derived self-assembly through coordination bonding between polyphenols and multivalent metal ions [11]. Nano- or micro-capsules with hollow metal-polyphenol structures can be obtained after removal of the template, and employed as drug delivery carriers to control cargo release [15]. Moreover, another assembly potential of plant polyphenol was found when exposed to polyphenol-rich beverages, involving unadulterated tea and wine. A more detailed investigation reported that plant polyphenol-inspired oxidative aggregates formed spontaneously at mildly alkaline pH (around 7–8) in the presence of oxygen [16]. Further research found that polyphenolic deposition offered a simple and versatile approach for surface modification [17], which has aroused broad interest in material engineering, biomedical science, etc. A recent study has applied oxidative self-polymerization properties to controlled drug delivery, using mesoporous silica nanoparticles as template materials to encapsulate drugs, yielding polyphenol-coated drug-loaded nanoparticles via autoxidation [18]. However, when used as delivery carriers, capsules with hollow structures must perform selective removal of templates after substance deposition. Direct deposit and *in situ* assemblies on the surface of hydrophobic drugs or nutraceutical nanoaggregates without any template, using polyphenol as the sole coating precursor, have been elusive, despite new opportunities for carrier-free nanostructured engineering materials to improve the loading capacity and bioavailability of targeted substances significantly.

Citrus polymethoxylated flavones is a unique class of natural bioactive substances. Among them, NOB has always received extensive attention due to its multi-functional pharmaceutical activities, including anti-inflammatory [19], anti-cancer [20], neuroprotection [21], etc. Notably, anti-cancer activity has received the most attention. Up to now, researchers have found that NOB has the potential to induce apoptosis with different signal pathways, especially for lung cancer [22], colon cancer [23], breast cancer [24], etc. Of note, the sensitivity of NOB varies with distinct cancer cell lines. Similar to inducing apoptosis, NOB can induce cell cycle arrest as well, including lung cancer [25]. It is worth noting that NOB shows anti-tumor invasion and metastasis activity with various cancer cells. For example, NOB can down-regulate the expression of MMP or up-regulate the expression of TIMP-1 in HT-1080 cells (human fibrosarcoma) to inhibit the migration and invasion tumor cells [26,27]. Interestingly, previous studies have proved that the combination of NOB with other bioactive substances endows complex a significant synergistic effect [28–30].

Herein, a natural carrier-free binary tannic acid-nobiletin nanoparticles (NT NPs) is self-assembled with green chemistry, which includes polyphenolic interfacial deposition and autoxidative self-polymerization, forming stable assemblies on NOB surfaces for controlled drug delivery. Interface assembly occurs immediately when mixing NOB nanoaggregates and TA in the aqueous solution successively. Dynamically changeable particle sizes appear, mainly regulated by hydrogen bonding and oxidation reaction, prior to reaching a steady state. Owing to the matched physicochemical properties, NT NPs induce apoptosis and inhibit tumor metastasis, ultimately displaying synergistic anti-tumor therapeutic effects. Overall, NT NPs have the broad potential to be designed as a valuable and versatile anti-tumor drug and provide a new vision to design binary carrier-free NPs in biological and pharmaceutical fields.

2. Material and methods

2.1. Materials

NOB (purity≥98 %) was purchased from the Shanxi HuiKe Botanical Development Co., Ltd. (Xi'an, China). TA and 3-(4,5-dimethylthiazol-2-yl)−2,5-diphenyltetrazolium bromide (MTT) were obtained from the Sigma-Aldrich. (St. Louis, USA). Acetonitrile (HPLC grade), acetic acid (HPLC grade), Dead Cell Apoptosis Kits and Cell Cycle Kit were procured from Thermo Fisher Scientific (Waltham, MA, USA). 3-Morpholinopropanesulfoinc acid (MOPS) was purchased from Genview (Houston, Texas, USA). Other chemicals of analytical grade were all purchased from Sinopharm Chemical Reagent Co., Ltd. (Shanghai, China). A Milli-Q water purification system (Millipore, USA) was used to prepare all aqueous solutions. In terms of cell culture, RPMI 1640 and DMEM/F12 were obtained from Life Technologies (Paisley, UK). Fetal bovine serum (FBS), trypsin, phosphate buffered saline (PBS), and penicillin-streptomycin (PS) were all purchased from Invitrogen (Carlsbad, CA, USA). H1299 cell was obtained from the Shanghai Institute of Biological Sciences (Shanghai, China) and cultured in RPMI-1640 media. HT1080 cell was purchased from the China Center for Type Culture Collection (Wuhan, China) and cultivated with DMEM/F12 medium. Both cell lines were incubated in a humidified incubator (Thermo Scientific, USA) with a humidified atmosphere of 5 % CO_2 and 37 °C.

2.2. Synthesis of NT complex particles

NOB stock solution (7 mg/ml, absolute ethanol) was added into 0.01 M MOPS buffer under vigorous stirring to obtain the final solution at pH 7.2. TA (24 mM, 150 μl) was then added with constant stirring for 10 s. The freshly prepared samples were put under 30 °C at a ventilated location for 0, 12 and 48 h prior to further use, and named NT0, NT12 and NT48, respectively. Correspondingly, blank T0, T12 and T48 solutions were fabricated with the same procedure, except that NOB was replaced with an equivalent amount of MOPS buffer.

2.3. Characterization of NT complex particles

Size distributions and zeta potential were measured by a Nano-ZS 90 Nanosizer (Malvern, UK). UV–vis absorption spectrum was determined by a UV–vis spectrophotometer (UV-2910, Japan). X-ray diffraction (XRD) spectrum was examined with an XRD diffractometer (D8-Advance, USA). Data were collected from 5° to 60° under 40 mA and 40 kV. Cu Kα was set as the pattern radiation. Fourier transform infrared (FTIR) spectrum was detected using a Jasco 4100 series (Jasco, Inc., USA). Polarizing microscope images were collected using a polarized light microscopy (Nikon D-Eclipse C1 80i, Japan). Morphological and structural characterizations were conducted with transmission electron microscope (TEM) (JEM-2100F, Japan) with a 100 kV accelerating voltage, scanning electron microscope (SEM) (S-4800, Japan) with a 5 kV accelerating voltage, and atomic force microscopy (AFM) (Bruker Multimode 8, USA). Coumarin-6 (0.2 mg/ml) was an alternative to NOB for confocal laser scanning microscope (CLSM) (Zeiss LSM 710, Germany) tests.

2.4. Simulations

Solute molecule parameters were generated from the General Amber Force Field (GAFF) [31], and the TIP3P water model [32] was employed. All simulations were performed with GROMACS (version 5.1.1) [33]. Periodic boundary conditions and the PME method were also applied in the simulations. The reference temperature was set at 303.15 K using a Nose-Hoover extended ensemble thermostat [34,35], and the reference pressure was set at 1 atm, coupled semi-isotropically using the Parinello-Rahman barostat [36,37] and a time constant of 5 ps. Bonds with H-atoms were constrained using the LINCS algorithm [38]. The simulation was carried out with a minimum of 50,000 steps, an equilibrium of 5 ns, and followed by production of 500 ns.

2.5. Determination of EE and LC

NOB was collected by ultrafiltration (8,000 rpm, 30 min). The separated liquid (free NOB) was mixed with DMSO and determined using high performance liquid chromatography (HPLC) (LC-2010C, Japan) with a mobile phase of acetonitrile/water containing 0.2 % of acetic acid at 70/30 (v/v). The UV detection wavelength was 329 nm with an optimal run duration of 20 min. NOB linear regression equation further calculated data, as shown in Fig. S10. Drug encapsulation efficiency (EE) and loading capacity (LC) were calculated as follows:

$$\text{EE (\%)} = [(\text{Amount of total added NOB} - \text{Free amount of NOB in NPs})/\text{Amount of total added NOB}] \times 100\ \%$$

$$\text{LC (\%)} = [(\text{Amount of total added NOB} - \text{Free amount of NOB in NPs})/\text{Amount of total NPs}] \times 100\ \%$$

2.6. Release kinetics studies

The following steps investigated the cumulative release of NOB from NT48 complex particles: NT48 or blank NOB solution (9 ml) was put into a dialysis bag (3.5 kDa) and immersed into 150 ml PBS buffer (pH 7.4, containing 2 % (w/v) Tween 80). At predetermined time intervals, 1 ml dialysate was tested by an HPLC with the same chromatographic conditions above. An equal volume of corresponding fresh media was added to maintain the sink condition.

2.7. MTT assay

Briefly, the targeted cells were plated at 1×10^4 cells/well in a 96-well plate and equilibrated for 24 h. The medium was then replaced by a fresh medium containing several experimental groups (naked NOB, NT48, and T48 complexes) under different concentrations. After another incubation of 24 h. MTT reagent was added before being cultured for another 4 h. DMSO was used to dissolve MTT-formazan, and the results were recorded by a microplate reader (Thermo Fisher Scientific, USA) at 490 nm. Cell viability was calculated as follows:

$$\text{Cell viability (\%)} = \frac{OD_{\text{sample}} - OD_0}{OD_{\text{control}} - OD_0} \times 100\%$$

where OD_{sample}, $OD_{control}$ and OD_0 represented the absorbance of tested, control and blank wells, respectively. Data were calculated as average ± SD ($n = 6$).

2.8. Cell apoptosis study

Briefly, cells were seeded into 6-well plates with 3×10^5 cells per well and incubated overnight. After treating different formulations for another 24 h, cells were harvested, washed 3 times by centrifugation, resuspended by Annexin V/FITC and propidium iodide (PI), and incubated for 15 min in the dark. Apoptosis was assessed using a flow cytometry (BD Biosciences, USA).

2.9. Cycle analysis

Cell processing protocol was similar to cell apoptosis study. The harvested cells were fixed and permeabilized with cold ethanol (75 %, v/v) overnight after washing with cold PBS three times. Cells were then harvested and stained with PI in the dark (15 min) before the measurement (flow cytometer, BD

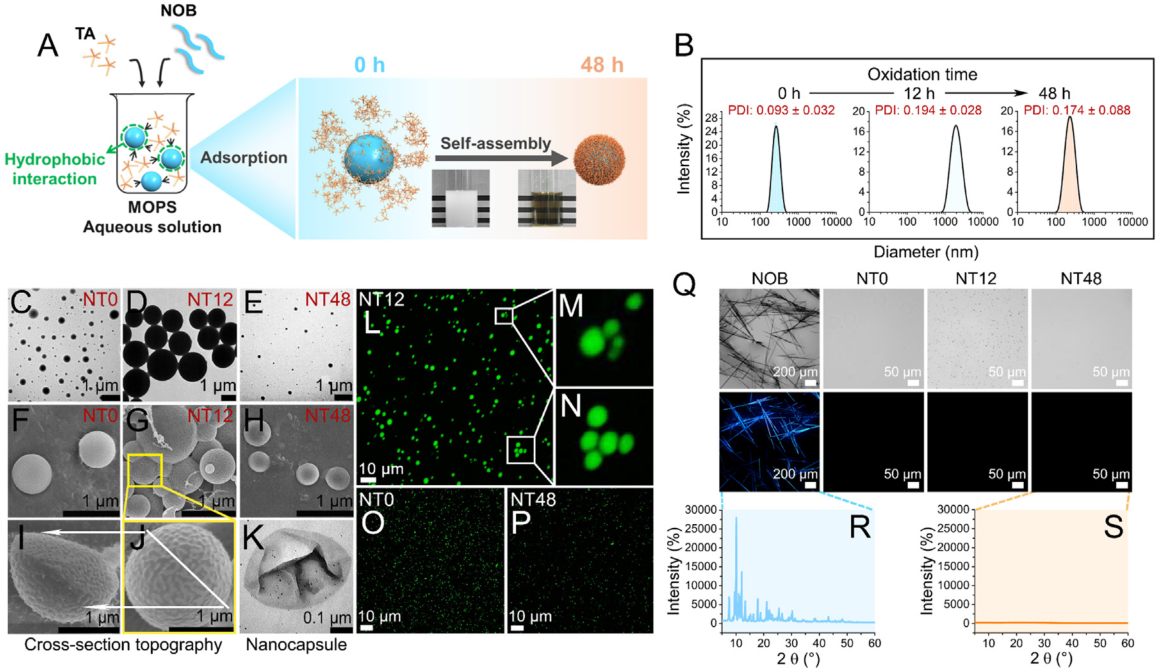

Fig. 1 – (A) Schematic illustration of NT0 and NT 48 NPs preparation process; (B) size distribution of NT0, NT12, and NT48 NPs; (C-E) TEM images of NT0, NT12, and NT48 NPs; (F-H) SEM images of NT0, NT12, and NT48 NPs; (I-J) non-cross section and cross section of SEM images of NT12 particles; (K) ethanol-etched T48 film; (L-P) CLSM images of coumarin-6-labelled NT0, NT12, and NT48 NPs; (Q) polarizing microscope images of NOB, NT0, NT12 and NT48 NPs; (R-S) XRDs of NOB and NT48 NPs; insert: photographs of NT0 and NT48 NPs.

Biosciences, USA). Each experimental group was conducted in triplicate. Data were analyzed by ModFit software.

2.10. *Wound healing assay*

Cells were seeded in 6-well plates for 24 h with an initial density of 5 × 10^5 cells per well. Next, the monolayer cells (almost 90 % of confluence) were scratched by pipette tips, followed by washing 3 times with PBS. Fresh serum-free mediums containing different treated groups were added to plates. The group only with fresh serum-free mediums was served as a control. The images were captured by an inverted optical microscope (Olympus, Japan), and results were further calculated by Image J software. The final NOB dosage was 8.75 mg/ml.

2.11. *Cell migration and invasion assay*

To evaluate cell migration and migration, we plated 5 × 10^4 H1299 and HT1080 cells in the serum-free medium into the top chamber of 24-well transwell chambers (pore size: 8 μm, Corning Costar, USA) with or without the pre-coating of Matrigel (BD Biosciences, USA). A complete medium (800 μl) containing 10 % (v/v) FBS was first added into lower chambers as a chemoattractant. After 24-h incubation with different treated formulations, cells that remained on the upper surfaces were carefully removed by a cotton swab. The migrated or invaded cells were fixed and stained with crystal violet (0.5 %, v/v) for 30 min, and further dissolved by acetic acid. Absorbance was measured by a microplate reader (Thermo Fisher Scientific, USA). The cell migration or invasion rate of different treatment groups was calculated by setting the control as 100 %.

2.12. *High-content imaging and elisa analysis*

We plated 5 × 10^3 H1299 cells per well in a 96-well plate and incubated them for 24 h. Different formulations were added for another 24-h treatment. The Opera Phenix High-Content Screening System (PerkinElmer, USA) recorded the real-time cell trajectory at predetermined time points. The data were further analyzed by Harmony software (PerkinElmer, USA). Cells were captured by staining cell nuclei with Hoechst 33342. The quantitative determination of protein levels was tested by the human ELISA kit according to the manufacturer's instructions.

2.13. *Western blot*

The cell pretreatment process was similar to the cell apoptosis study. The harvested cells were lysed with RIPA buffer. Subsequently, protein lysates were separated using SDS-PAGE (Beyotime, China), followed by a transfer to the PVDF membrane. The membrane was then blocked with 5 % non-fat milk for approximately 1 h prior to incubation with primary antibody (1:1,000 dilution, Invitrogen) at 4 °C overnight. After washing, the membrane was incubated with secondary antibodies (1:4,000, Invitrogen) for an additional 1 h. According

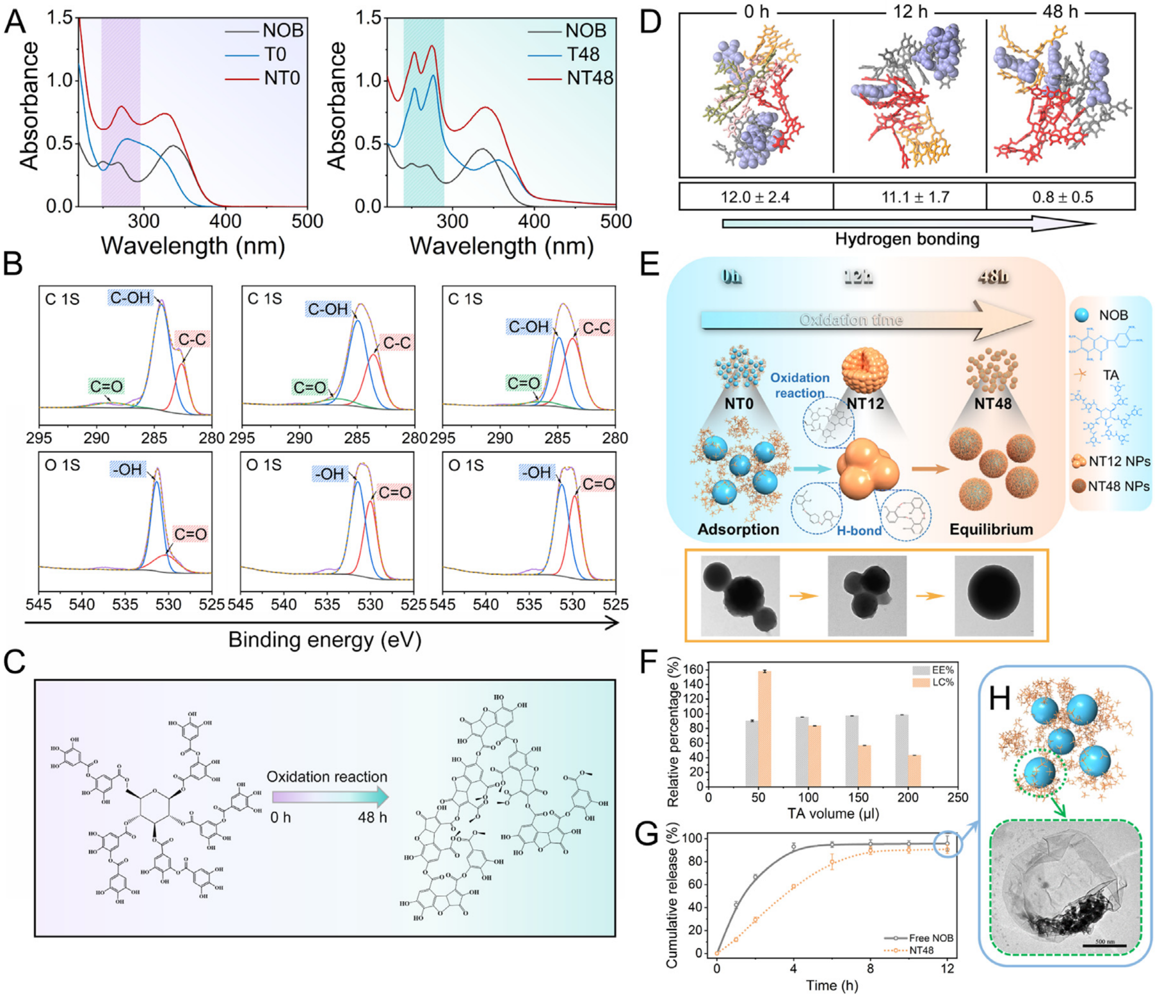

Fig. 2 – (A) UV–Vis spectrum of NT0 and NT48 NPs; (B) XPS analysis of NT0, NT12, and NT48 NPs; (C) molecular structure formula of tannic acid before and after oxidation; (D) hydrogen bonds and binding sites of TA on NOB (blue) coarse grains; (E) schematic diagram of the mechanism of changeable particle sizes with prolonged oxidative time; (F) encapsulation efficiency and loading capacity with different volume of TA; (G) NOB release curve from NT48 NPs at pH 7.4; (H) TEM images of degradable NT48 NPs.

to the manufacturer's protocol, a chemiluminescence system finally detected the signals (Thermo Scientific, MA, USA). β-actin (1:4,000, Invitrogen) served as the control.

2.14. *In vivo anti-tumor activity*

Ethical approval was obtained from the Lab of Animal Experimental Ethical Inspection of the Laboratory Animal Centre, Huazhong Agriculture University with the assigned approval number: HZAUMO-2020–0076. BALB/c nude mice (male, 3–4 week) were obtained from the Beijing Vital River Laboratory Animal Technology Co., Ltd. (Beijing, China). All mice were randomly assigned to four groups (Control, NOB, N48 NPs, and T48 complexes), raised under SPF conditions, and received care according to the guidelines of the Committee on Animal Research and Ethics. A subcutaneous transplantation tumor model was established by injecting 5×10^6 H1299 cancer cells into the right flank of each mouse. Different formulations were intratumorally injected with a final NOB dosage of 35 μg/ml in PBS. All treatments (0.1 ml) were performed 2 d per time. Tumor volume and body weight in all cases were monitored every day during the experiment, and tumor volume was calculated by the following formula:

$$\text{Tumor volume} = \text{Length} \times \text{Width}^2/2$$

At 30-d post-injection, mice were euthanized. The tumor and other main organs were excised, weighed, and fixed in 10 % formalin for further TUNEL assay, hematoxylin and eosin (H&E) staining, and immunohistochemical analysis. The tumor inhibition rate (TIR) was calculated by the following equation:

$$\text{TIR (\%)} = \frac{C_0 - C_{\text{sample}}}{C_0} \times 100\%$$

where C_0 and C_{sample} represented the average tumor volume of the control group and the experimental group, respectively.

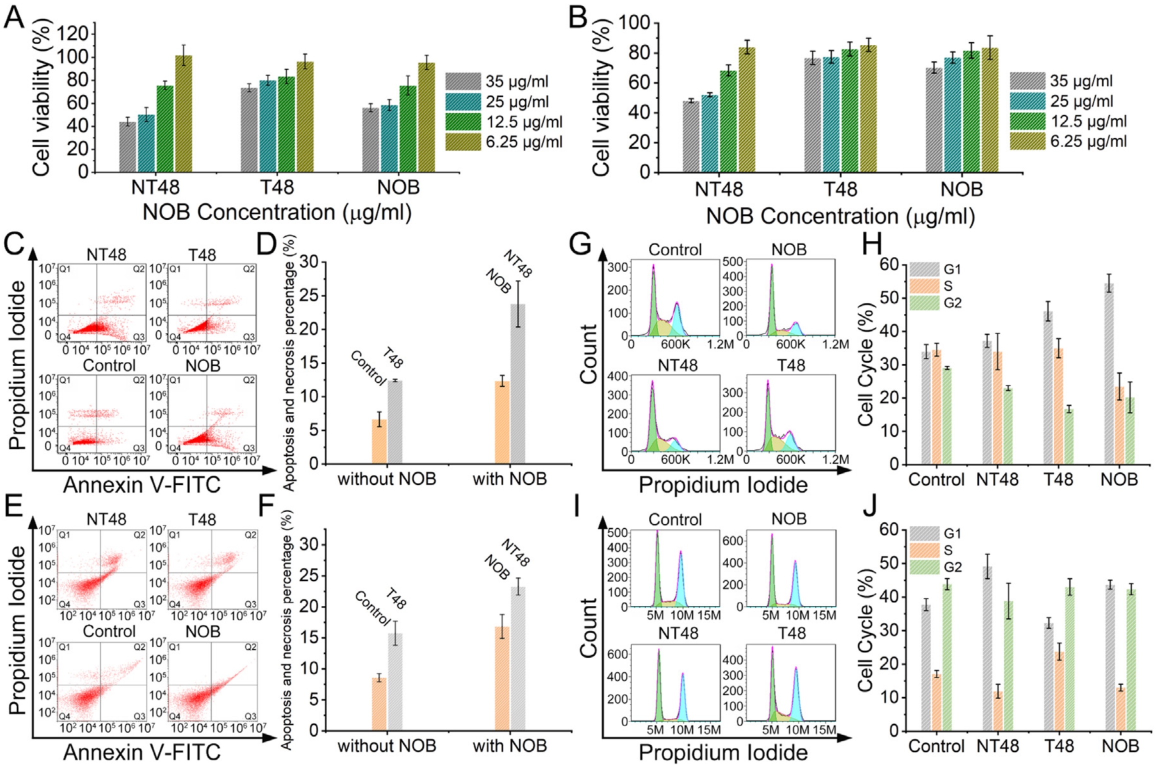

Fig. 3 – *In vitro* anti-cancer activity assay. (A-B) Cell viability (MTT assay); (C-F) Cell apoptosis; (G-J) Cell cycle assay of H1299 (A, C-D, G-H) and HT1080 (B, E-F, I-J) cell lines with formulation of Control, NOB, NT48 and T48 complex NPs for different NOB dosages after the incubation time of 24 h. The measurements were conducted in triplicate ± SD.

2.15. *Immunohistochemical staining*

Immunohistochemical analysis of caspase-3, PARP1, Ki-67 and PCNA were performed using rabbit monoclonal antibodies against caspase-3 and C-PARP1 (Abcam, USA), and mouse monoclonal antibodies against Ki-67 (Novus, USA) and PCNA (Boster, China), followed by incubation with biotin-labelled secondary antibody. Immunohistochemical images were captured by an optical microscope (CX-21, Olympus).

2.16. *Statistical analysis*

All data are presented as mean ± SD. Statistical analysis was conducted by IBM SPSS Statistics 24 software. ANOVA and Student's t-test were used for multiple comparisons. Statistical differences were defined as follows: $^{*}P < 0.05$, $^{**}P < 0.01$, and $^{***}P < 0.001$.

3. Results and discussion

3.1. *Synthesis and characteristics of NT NPs*

Hydrophobic NOB nanoaggregates are engineered by dropping NOB solution (dissolved in ethanol) into MOPS aqueous solution to undergo an antisolvent step, which provides sufficient space for polyphenolic deposition and the subsequent *in situ* self-assembly of NPs (Fig. 1A). Unexpectedly, when the fabricated NPs are put under 30 °C at a ventilated location, the color change phenomenon occurs. To explain this phenomenon, a more systematic and in-depth study is conducted in Fig. S1. Results showed that the color changes from white to brown with increasing incubation time (0–48 h). Meanwhile, the initial white solution becomes opaque with increasing incubation time to 12 h. Then, the opaque solution gradually becomes transparent during 12 to 48 h. Ultimately, a brown but transparent solution is formed after 48 h. Specifically, we select three critical time points of 0, 12 and 48 h in the following experiment, and the corresponding NPs are termed NT0, NT12 and NT48, respectively.

Analysis of the assembled nano-dispersions shows similar monomodal distributions in all treated time points (Fig. 1B). Notably, the diameter of NT0 NPs (247 ± 20 nm) increases gradually and reaches the maximum value of ~1,818 nm at ~12 h. On the contrary, an opposite decreasing trend occurs with continuously incubating time until a steady-state after 48 h (206 ± 5 nm) (Fig. 1B). In addition, a similar size tendency appears again, irrespective of changes in TA or NOB dose (Fig. S2-S3). Interestingly, three NT particles display predominantly round and full spheres with different dimensions (Fig. 1C-1H). The differences, however, are that NT0 and NT48 particles exhibit monodisperse nanospheres, while NT12 is more likely to aggregate. Confocal laser scanning microscopy (CLSM) images (Fig. 1L-1P) also verify this phenomenon. It is worth noting that the rough surface of NT12 particles seems to be composed of considerably small, but round, spheres (Fig. 1J).

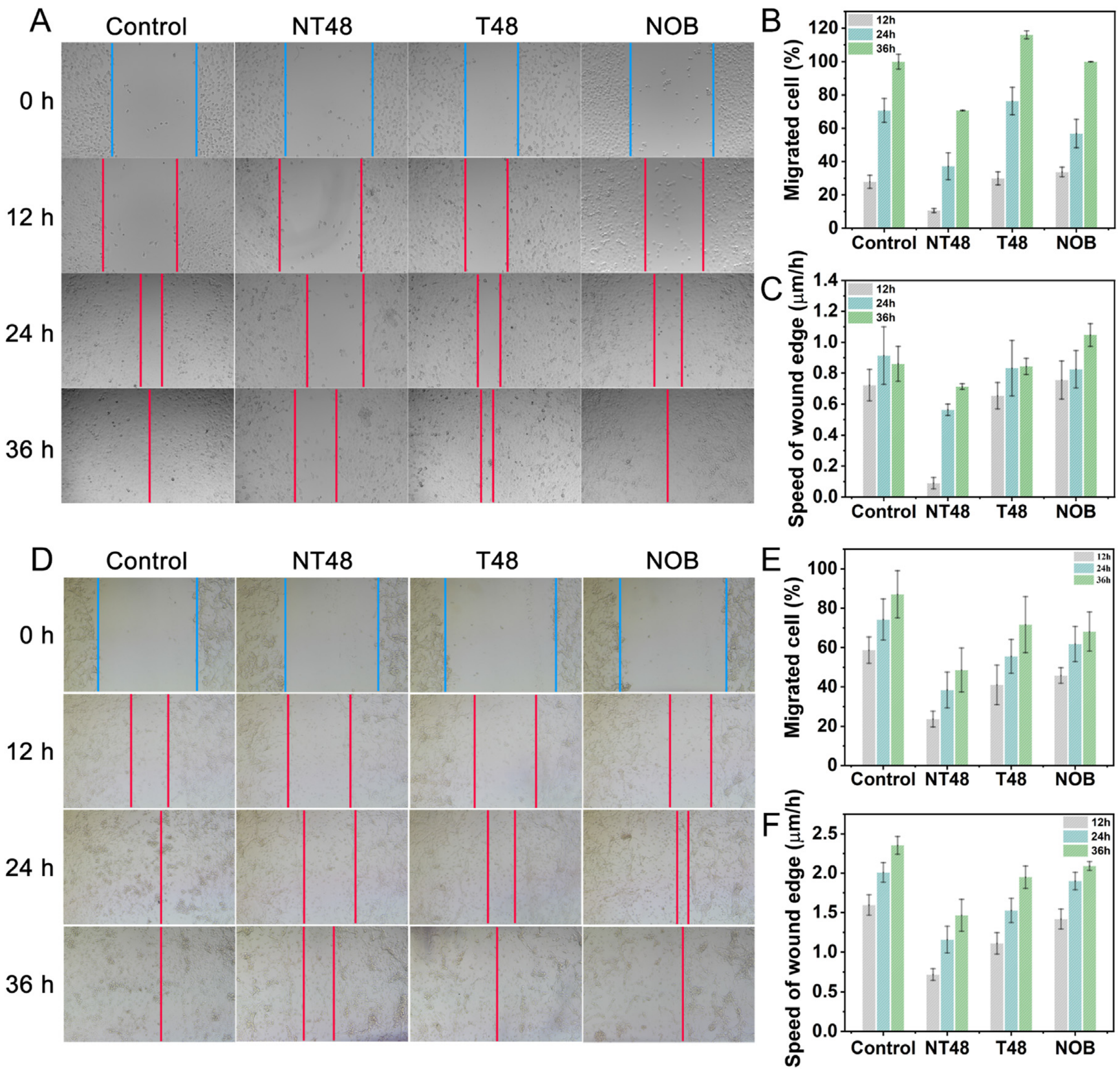

Fig. 4 – Wound healing assay and the corresponding quantitative analysis of H1299 (A-C) and HT1080 (D-F) cell lines with formulation of Control, NOB, NT48 and T48 complex NPs for different NOB dosages after the incubation time of 0, 12, 24 and 36 h. Data shown as mean ± SD, *n* ≥ 6.

A highly similar cross-section topography is also observed in Fig. 1I. Therefore, it is determined that a large number of small particles make up the whole NT12 complexes. To further explore the existing state of the polyphenol module on the drug surface, we attempt to remove NOB from NT48 NPs and obtain an obvious intact hollow nanocapsule at the end (Fig. 1K). Clearer confirming observations about this intact hollow capsule are further captured, with PS microspheres as a substitute for NOB nanocores to avoid intermolecular forces (Fig. S4C- S4E). These findings indicate that our assembled NPs possess a unique core-shell structure.

As observed in Fig. 1Q and S5, the pure NOB sample exhibits a prominent needle crystal structure, while crystallization is not visible in NT48 particles. More convincing results are found in the XRD pattern. The naked NOB displays numerous sharp Bragg peaks, attributed to the highly crystalline property [39]. These peaks, however, almost disappear after being incorporated into NT48 particles (Fig. 1R and 1S). Classical nucleation and growth theory reveals that some small crystalline nuclei can form at first prior to growing and agglomerating into final crystalline particles. Nevertheless, if the system reaches a high supersaturation level before crystallization, the crystallizable molecule can precipitate as metastable nanoclusters directly [40]. Here, NOB acts as a crystalline nucleus and tends to interact with TA molecules via their strong anchoring, eventually leading to imperfect crystallization. This conclusion is further verified by DSC measurement, accompanied by broadened and shifted endothermic and crystallization peaks (Fig. S6), corresponding to the imperfect crystallinity of NOB.

3.2. *Structural mechanism for the formation of NT NPs*

Insight into the structural organization and formation mechanism can provide necessary guidance for optimal designing and engineering nanoscale delivery systems. The

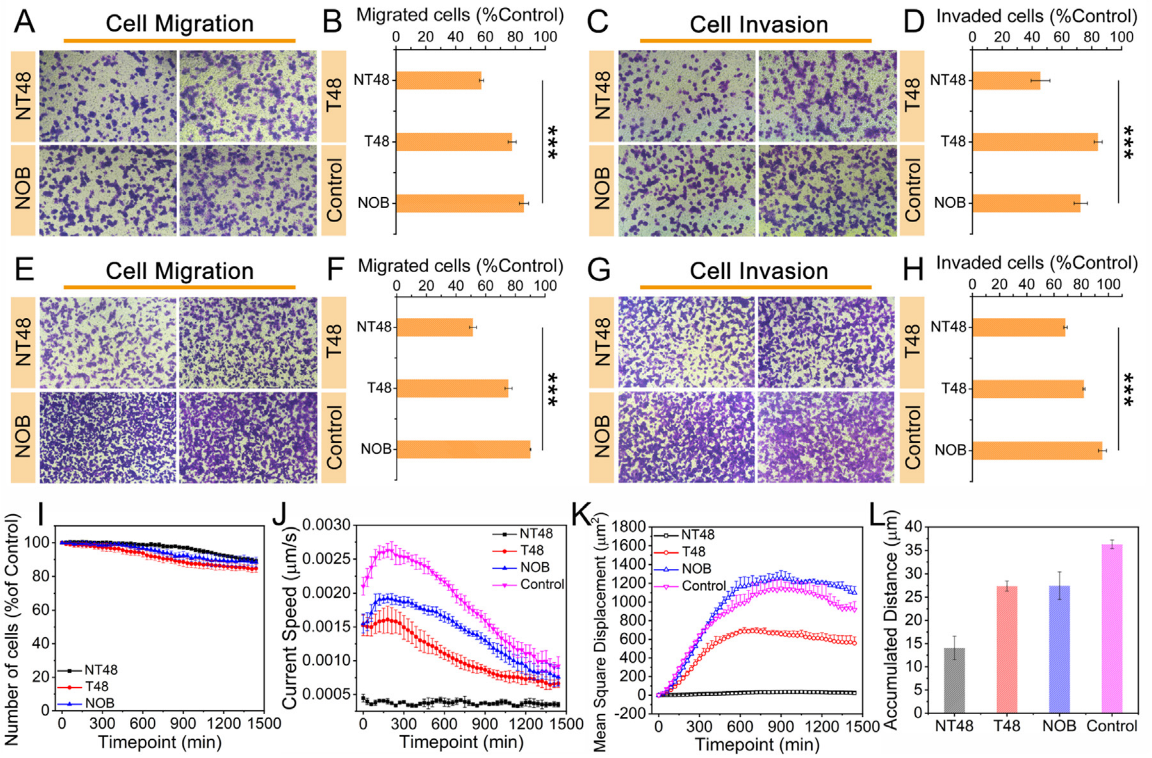

Fig. 5 – *In vitro* anti-metastasis ability evaluation. (A-H) Transwell migration assay and invasion assay and their corresponding quantitative analysis of H1299 (A-D) and HT1080 (E-H) cell lines. High-content imaging analysis of cell number (I), accumulated (J), mean migratory distance (K), and migratory speed (L) of H1299 cell line with the formulation of Control, NOB, NT48, and T48 complex NPs for different NOB dosages after an incubation time of 24 h. Data shown as mean ± SD, two-way ANOVA, ***P < 0.001, *n* ≥ 3.

UV–Vis results reveal that the characteristic absorption band of TA at 276 nm is transformed into another two new peaks (253 and 275 nm) after incubating for 48 h (Fig. 2A), corresponding to the formed benzoquinone via oxidation reaction [41–43]. Therefore, the oxidation reaction appears presumably in the final system, which is further confirmed by determining the C 1 s and O 1 s photoelectron spectra using XPS (Fig. 2B). The diminished hydroxyl group peak, synchronously accompanied by the increasing carbonyl peak, proves the successful conversion from the catechol or galloyl group into quinone during the autoxidation reaction of TA [18,44]. These results suggest that phenolic deprotonation via autoxidation is a primary interaction force in our system (Fig. 2C) [45].

In addition, the existence of hydrogen bonding in NT0 NPs is verified by the FTIR spectrum, with the characteristic peak hydroxyl groups shifting from 3346 cm^{-1} to 3423 cm^{-1} (Fig. S7), which is also further confirmed by the fact that urea can break the NT0 system (Fig. S8) [46–49]. Notably, simulation verifies that the number of hydrogen bonds decreases during the oxidative process (Fig. 2D and S9). Taken together, we postulate that the formation process of NT NPs not only primarily relies on the autooxidation reaction of TA, but also requires a certain degree of hydrogen bond cross-linking. More importantly, it is plausible that the hydrogen bonding causes NT particles to aggregate, accompanied by a gradually increasing particle size during the first 12 h. Meanwhile, the autoxidation reaction forms a stable film to prevent NOB from crystallizing (Fig. 2E). The weak alkaline environment continuously weakens hydrogen bonding forces between particles and finally leads to the depolymerization of NT12 NPs.

EE and LC are essential in effective drug delivery and anti-cancer therapy [50]. In our case, all EE values are >90 % (Fig. 2F), and even up to 98.5 % with the initial TA volume of 200 μl. EE is used to evaluate the proportion of loaded drugs to totally added drugs. This high EE is vital for improving the solubility and stability of poor-soluble drugs [51]. LC values are even up to 160 % in the NT48 complex NPs, depending on the initial TA concentration (Fig. 2F). Of note, LC represents the proportion of loaded drugs to other ingredients. This high LC corresponds to a better economy, with less embedding material, and has the potential to endow our fabricated NPs with promising therapeutic effects along with minimized side effects in drug delivery [52]. A burst release profile is found in the pure NOB group, as drug particles close to the surface are easily accessible by hydration [53]. In contrast, NT NPs exhibited a relatively slow release phase, during which the NOB molecule diffuses slowly through a few existing pores of the dense TA oxidative layer, accompanied by carrier degradation and hydration [54] (Fig. 2G). Besides, this good dissolution behavior, presumably also ascribed to the mesocrystal nature of NOB

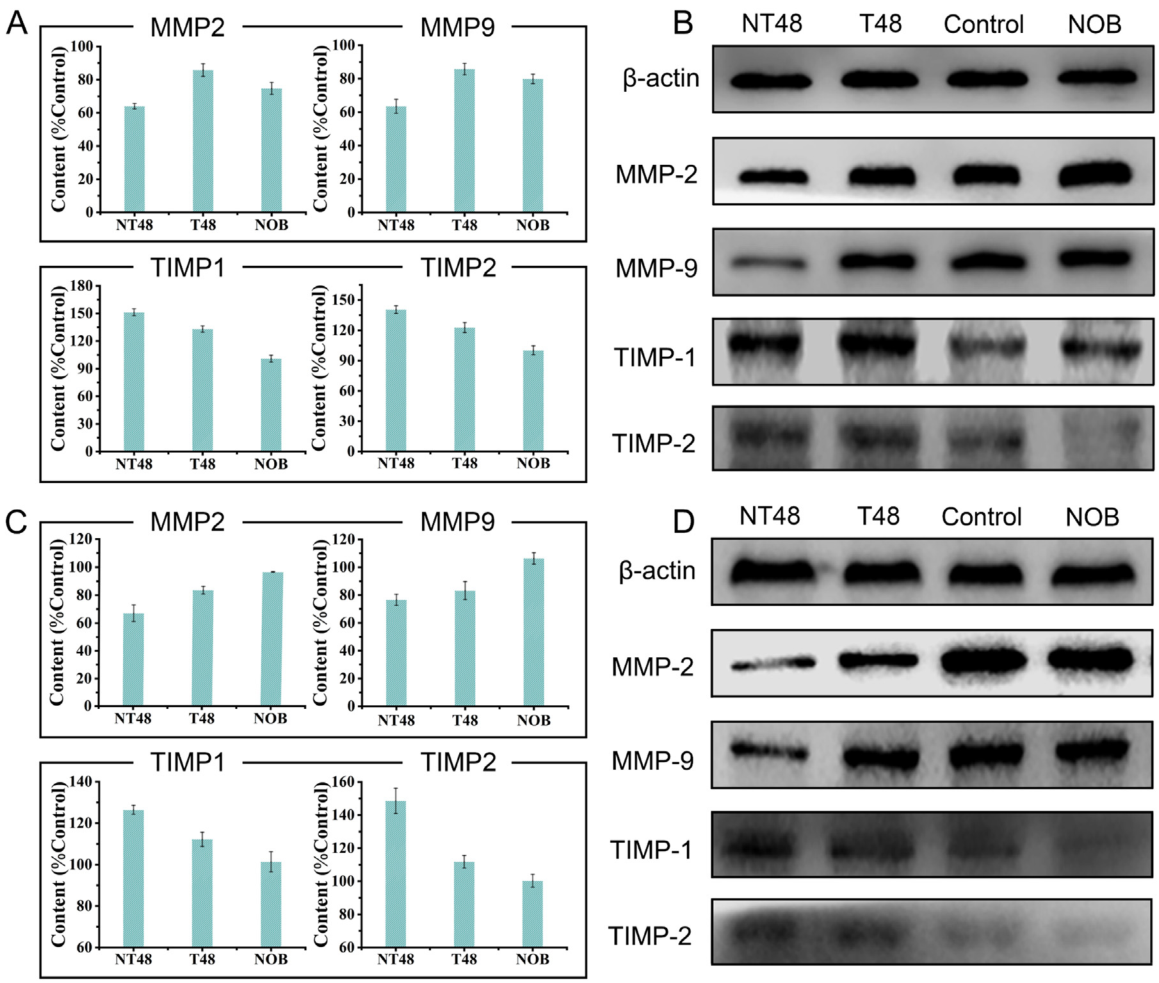

Fig. 6 – Elisa assay (A, C) and Western blot analysis (B, D) of H1299 (A-B) and HT1080 (C-D) cell line.

when incorporated into the complex NPs, is also beneficial in improving their bioavailability [55]. Capsule-like topography with drugs incorporated is confirmed again at the end of the release (Fig. 2H).

3.3. *Synergistic anti-cancer activity in vitro of NT48 NPs*

MTT assay results from Fig. 3A-B illustrate that individual TA has some anti-cancer effects at high NOB dosages of 35 μg/ml (cell viability: 73 % for H1299 cells and 77 % for HT1080 cells), mostly due to its excellent biological functions. It is noteworthy that the naked NOB group exhibits slight toxicity only at high dosages, because the biological efficacy is limited by its strong hydrophobicity. Whereas, the NT48 formulation exhibits severe cytotoxicity in a dosage-dependent manner, presumably illustrating a predominant combination efficacy of NOB and T48 complexes in both H1299 and HT1080 cell lines. Annexin V-FITC/PI staining assay is further conducted to examine the tumor suppressive ability (Fig. 3C for H1299 cell line, Fig. 3E for HT1080 cell line). The treatment with NOB-loaded NT48 NPs remarkably upregulates cell apoptosis. To quantify these differences, the apoptosis and necrosis rates are also calculated in Fig. 3D and 3F, confirms superior cell apoptosis of NT48 NPs again. The apoptosis mentioned above is presumably due to the fact that some apoptotic body protein complexes (cytochrome C, caspase-9 protein precursors, etc.) and apoptosis initiation enzymes (caspase-9) are activated, followed by the initiation of downstream effector enzymes (such as caspase-3), which eventually leads to apoptosis [56]. Cell cycle results indicate that the NOB-based system arrests cells at the G1 phase due to NOB biological activity (Fig. 3G-H and 3I-3 J).

More important, results point out our NT48 NPs lead to a significant inhibitory effect on tumor metastasis, even under a non-toxic NOB concentration (8.75 µg/ml), in comparison with the corresponding free NOB ($P < 0.001$) in both H1299 and HT1080 cell lines. We first carry out transwell assay to evaluate their anti-migration and invasion behaviors. Interestingly, compared to the control group, ~42.7 % H1299 cells and ~48.7 % HT1080 cells are arrested by NT48 NPs, superior to those treated with the corresponding free NOB ($P < 0.001$) (Fig. 5A-5B and 5E-5F). Results from Fig. 5C-5D and 5G-5H also highlight the superior anti-invasion effect of NT48 NPs. Wound-healing assay (Fig. 4) and high-content imaging analysis confirm the limited migratory distance and speed under this non-toxic concentration (Fig. 5I) of NT48 NPs,

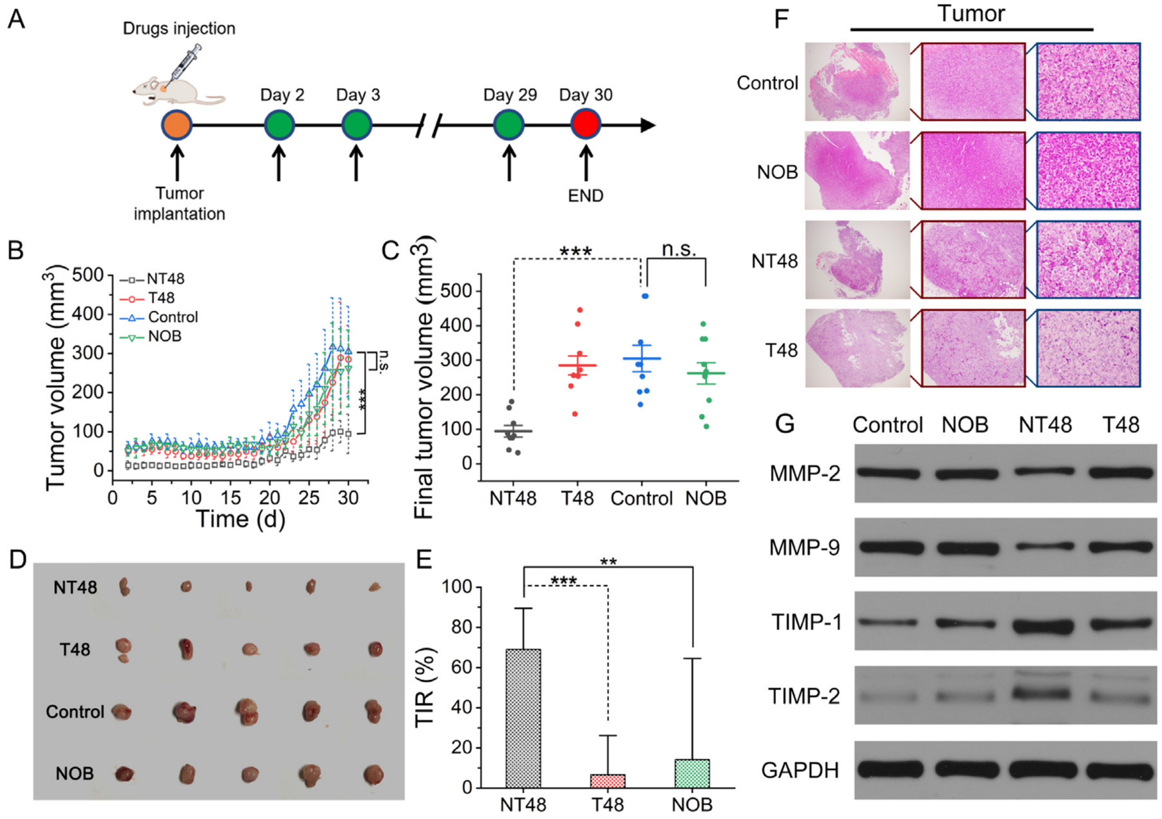

Fig. 7 – *In vivo* anti-tumor activity evaluation. (A) Schematic illustration of the establishment of H1299 lung xenograft tumor model; (B) tumor volume change; (C) final tumor volume; (D) images of resected tumors; (E) TIR; (F) histology images of tumors (H&E staining); (G) Western blot analysis of BALB/c nude mice against H1299 lung xenograft tumors receiving different treatments (Control, NOB, NT48 NPs and T48 NPs). Data shown as mean ± SD, two-way ANOVA, *$P < 0.05$; **$P < 0.01$; ***$P < 0.001$ vs. NOB group, $n \geq 5$.

with naked NOB as a control (Fig. 5J-5L). This was probably attributed to the fact that our fabricated NT48 NPs can inhibit the expression of MMP2 and MMP9, and promote the expression of TIMP1 and TIMP2, as determined by both Elisa assay and Western blot analysis (Fig. 6). Previous studies have reported that MMPs family are closely related to cancer invasion, due to their degradative capacity for extracellular matrix. Such capacity enables cancer cells to migrate and colonize host tissues [57]. In particular, MMP9 has the great potential to degrade basement membrane components, which is associated with cancer metastasis and invasion [56]. Notably, the expression of MMPs can be effectively restrained by its natural inhibitor called TIMPs [58]. Hence, it is worth mentioning that downregulating the expression of MMPs and upregulating the expression of TIMPs are crucial for anti-migration and anti-invasion effects.

3.4. *In vivo anti-tumor efficacy of NT48 NPs*

Motivated by the highly efficient *in vitro* anti-cancer activity of NT48 NPs, *in vivo* anti-tumor efficacy is evaluated by an H1299 human tumor xenograft model (Fig. 7A). Results show that the tumor volume of the Control group increases rapidly (Fig. 7B). 30 d of free NOB or T48 treatment alone only slightly inhibits the growth of the primary tumor (Fig. 7B and 7D), with a TIR of 8 % and 15 %, respectively (Fig. 7E). The NT48 NPs show striking anti-tumor activity, reaching a high TIR of ~70 % under a corresponding concentration of NOB, where the significant anti-tumor effect begins on Day 2 (Fig. S11), and it remains until the end of the experiment (Fig. 7B). Pathological analysis of tumor tissues in Fig. 7F is performed after the observation period, treated with our formulation (Control, NOB, NT48 NPs and T48 NPs). Notably, Western blot results show that the protein expression levels in Fig. 7G are in line with the results in Fig. 6. No noticeable body weight change (Fig. S12) is found in all treatment groups, indicating the low systemic toxicity of our formations. Moreover, no significant lesion is observed in the histopathological examination of the major organs (Fig. S13), indicative of negligible toxic side effects of NT48 NPs. Immunohistochemical stainings reveal that the number of TUNEL+ and caspase-3+ cells in the NT48 NPs group is dramatically elevated (Fig. 8), indicative of enhanced apoptosis. Whereas, Control and NOB groups display a decrement in these positive cells. Likewise, cleaved PARP staining result confirms that, although a slight increase occurs in the percentage of apoptosis in the T48 group, the NT48 group still exhibits the largest area of apoptosis. Analyses of Ki67 and PCNA show the cell proliferation index in all treatment groups. Similar expressions of Ki67+ and PCNA+ cells are displayed in both Control and NOB groups, indicating the minor inhibitory effects on tumor proliferation *in vivo*. By contrast, NT48 NPs result in a significant decrease in Ki67- and

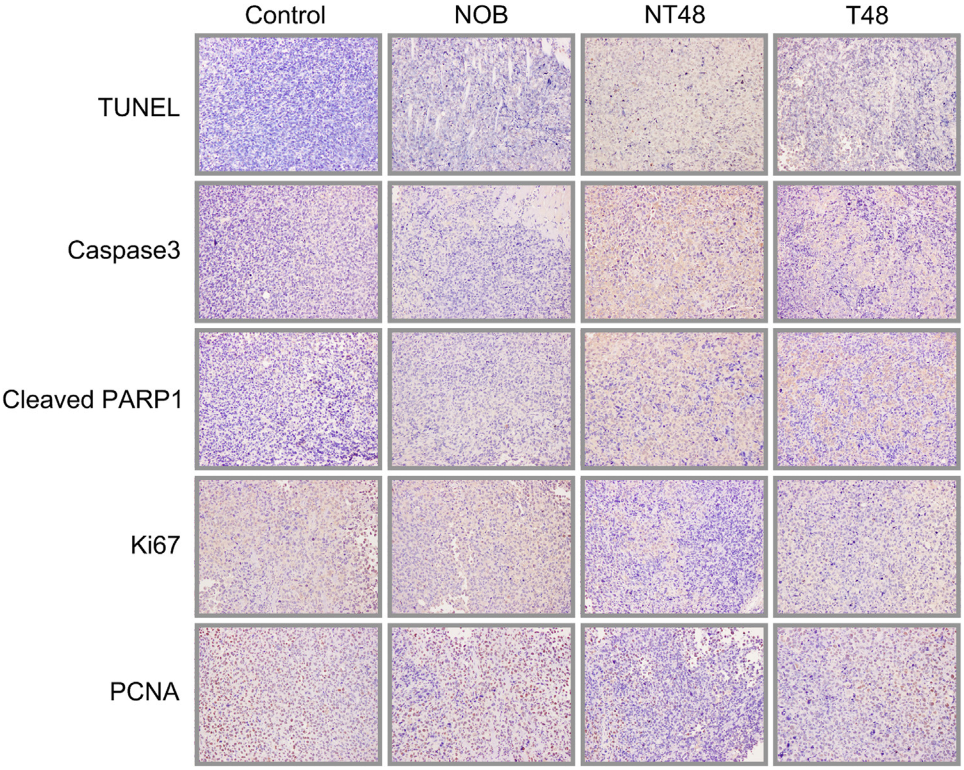

Fig. 8 – Immunohistochemical analysis of TUNEL, caspase-3, cleaved PARP1, Ki67 and PCNA of tumor tissue slices after various treatments.

PCNA-positive cells, due to the inhibition of cell proliferation. Collectively, it can be concluded that the potent encapsulation of hydrophobic drug (NOB) into NT48 NPs can indeed promote its bioavailability, which endows NT48 NPs to be an efficient agent to induce tumor apoptosis and suppress tumor growth *in vivo*.

4. Conclusion

In this paper, high-loading capability and carrier-free nanoparticles are self-assembled by natural compounds TA and NOB. During the particle self-assembled process, an interesting color change phenomenon occurs, accompanied by controllably and dynamically changing particle sizes. Briefly, the initial white and opaque solution becomes brown but transparent in the end. Meanwhile, the diameters of particle sizes increase gradually in the first 12 h. On the contrary, an opposite decreasing trend occurs with continuously incubating time from 12 to 48 h. Ultimately, uniform and spherical NT48 NPs occur in a stable state, enabling incorporated drugs to preserve their function and be suitable for drug delivery. Comprehensive multi-spectroscopy studies and molecular dynamics simulations reveal that this assembly strategy includes interfacial deposition and *in situ* self-polymerization among phenolic building blocks, involving hydrogen bonding, oxidative reactions, etc. Results showed that the formed NT48 NPs can effectively inhibit NOB crystallization and further improve the bioavailability of poorly water-soluble NOB. Moreover, the combination of TA and NOB endows NT48 NPs with a synergistic anti-tumor effect. *In vitro* and *in vivo* evaluations demonstrate that the NT48 NPs impart an apparent cytotoxic effect and highly efficient anti-metastatic effect on target cancer cells. Taken together, our natural small molecule carrier-free NT48 NPs are clinically promising as an effective anti-tumor therapy, as they have appropriate size, extremely high drug loading capacity and excellent biological activity. Moving forward, further research is imperative to design our delivery NPs with specificity to target cells and controlled drug release at the target site. Meanwhile, our delivery material needs to be further assessed in pharmacokinetics and biodistribution for innovation and development of advanced functional biomaterials.

Declaration of Competing Interest

The authors declare that they have no known competing financial interests or personal relationships that could have appeared to influence the work reported in this paper.

Acknowledgments

This work was financially supported by the Knowledge Innovation Program of Wuhan-Shuguang Project (Project No: 2022020801020233) and the Key R&D Program of Wuhan City in China (2023020402010600). We express sincere gratitude to Jingnan Ren of the Key Laboratory of Environment

Correlative Dietology of Huazhong Agricultural University for her invaluable assistance and the Scientific Center for Optical and Electron Microscopy (ScopeM) of ETH Zurich. Finally, we thank Prof. Raffaele Mezzenga for his invaluable facilities' support.

Supplementary materials

Supplementary material associated with this article can be found, in the online version, at doi:10.1016/j.ajps.2024.100992. The figures and tables with "S" before the serial number are included in the Supplementary material.

References

[1] Liang H, Bin Z, Wu D, Li J, Li B. Supramolecular design and applications of polyphenol-based architecture: a review. Adv Colloid Interface Sci 2019:102019.

[2] Xu LQ, Neoh KG, Kang ET. Natural polyphenols as versatile platforms for material engineering and surface functionalization. Prog Polym Sci 2018;87:165–96.

[3] Guo Y, Sun Q, Wu FG, Dai Y, Chen X. Polyphenol-containing nanoparticles: synthesis, properties, and therapeutic delivery. Adv Mater 2021;33(22):2007356.

[4] Kim S, Kim DS, Kang SM. Reversible layer-by-layer deposition on solid substrates inspired by mussel byssus cuticle. Chem Asian J 2014;9(1):63–6.

[5] Wang J, Zheng S, Liu J, Xu Z. Tannic acid adsorption on amino-functionalized magnetic mesoporous silica. Chem Eng J 2010;165(1):10–16.

[6] Hu S, Wang T, Fernandez ML, Luo Y. Development of tannic acid cross-linked hollow zein nanoparticles as potential oral delivery vehicles for curcumin. Food Hydrocoll 2016;61:821–31.

[7] Liang H, Zhou B, Li J, Xu W, Liu S, Li Y, et al. Supramolecular design of coordination bonding architecture on zein nanoparticles for pH-responsive anticancer drug delivery. Colloids Surf B 2015;136:1224–33.

[8] Thongkaew C, Gibis M, Hinrichs J, Weiss J. Polyphenol interactions with whey protein isolate and whey protein isolate-pectin coacervates. Food Hydrocoll 2014;41:103–12.

[9] Ju Y, Cui J, Muellner M, Suma T, Hu M, Caruso F. Engineering low-fouling and pH-degradable capsules through the assembly of metal-phenolic networks. Biomacromolecules 2015;16(3):807–14.

[10] Kim YJ, Uyama H, Kobayashi S. Enzymatic template polymerization of phenol in the presence of water-soluble polymers in an aqueous medium. Polym J 2004;36(12):992–8.

[11] Ejima H, Richardson JJ, Liang K, Best JP, van Koeverden MP, Such GK, et al. One-step assembly of coordination complexes for versatile film and particle engineering. Science 2013;341(6142):154–7.

[12] Guo J, Ping Y, Ejima H, Alt K, Meissner M, Richardson JJ, et al. Engineering multifunctional capsules through the assembly of metal-phenolic networks. Angew Chem 2014;126(22):5652–7.

[13] Liang H, Pei Y, Li J, Xiong W, He Y, Liu S, et al. pH-Degradable antioxidant nanoparticles based on hydrogen-bonded tannic acid assembly. RSC Adv 2016;6(37):31374–85.

[14] Yi X, Chen Y, Ding B, Ma K, Li Z, Luo Y. High internal phase Pickering emulsions prepared by globular protein-tannic acid complexes: a hydrogen bond-based interfacial crosslinking strategy. J Mol Liq 2023;370:121025.

[15] Ju Y, Cui J, Sun H, Mullner M, Dai Y, Guo J, et al. Engineered metal-phenolic capsules show tunable targeted delivery to cancer cells. Biomacromolecules 2016;17(6):2268–76.

[16] Sileika TS, Barrett DG, Zhang R, Lau KHA, Messersmith PB. Colorless Multifunctional coatings inspired by polyphenols found in tea, chocolate, and wine. Angew Chem 2013;52(41):10766–70.

[17] Hong S, Yeom J, Song IT, Kang SM, Lee H, Lee H. Pyrogallol 2-Aminoethane: a plant flavonoid-inspired molecule for material-independent surface chemistry. Adv Mater Interfaces 2014;1(4):1400113.

[18] Li J, Wu S, Wu C, Qiu L, Zhu G, Cui C, et al. Versatile surface engineering of porous nanomaterials with bioinspired polyphenol coatings for targeted and controlled drug delivery. Nanoscale 2016;8(16):8600–6.

[19] Wang SW, Lan T, Sheng H, Zheng F, Lei MK, Wang LX, et al. Nobiletin alleviates non-alcoholic steatohepatitis in MCD-induced mice by regulating macrophage polarization. Front Physiol 2021;12:687744.

[20] Ashrafizadeh M, Zarrabi A, Saberifar S, Hashemi F, Hushmandi K, Hashemi F, et al. Nobiletin in cancer therapy: how this plant derived-natural compound targets various oncogene and onco-suppressor pathways. Biomedicines 2020;8(5):110.

[21] Matsuzaki K, Ohizumi Y. Beneficial effects of citrus-derived polymethoxylated flavones for central nervous system disorders. Nutrients 2021;13(1):145.

[22] Moon JY, Manh Hung LV, Unno T, Cho SK. Nobiletin enhances chemosensitivity to adriamycin through modulation of the Akt/GSK3β/β^{-}catenin/MYCN/MRP1 signaling pathway in A549 human non-small-cell lung cancer cells. Nutrients 2018;10(12):1829.

[23] Wu X, Song M, Wang M, Zheng J, Gao Z, Xu F, et al. Chemopreventive effects of nobiletin and its colonic metabolites on colon carcinogenesis. Mol Nutr Food Res 2015;59(12):2383–94.

[24] Liu J, Wang S, Tian S, He Y, Lou H, Yang Z, et al. Nobiletin inhibits breast cancer via p38 mitogen-activated protein kinase, nuclear transcription factor-κB, and nuclear factor erythroid 2-related factor 2 pathways in MCF-7 cells. Food Nutr Res 2018;62:1323.

[25] Uesato S, Yamashita H, Maeda R, Hirata Y, Yamamoto M, Matsue S, et al. Synergistic antitumor effect of a combination of paclitaxel and carboplatin with nobiletin from Citrus depressa on non-small-cell lung cancer cell lines. Planta Med 2014;80(6):452–7.

[26] Sato T, Iwai M, Sakai T, Sato H, Seiki M, Mori Y, et al. Enhancement of membrane-type 1-matrix metalloproteinase (MT1-MMP) production and sequential activation of progelatinase A on human squamous carcinoma cells co-cultured with human dermal fibroblasts. Br J Cancer 1999;80(8):1137–43.

[27] Miyata Y, Sato T, Imada K, Dobashi A, Yano M, Ito A. A citrus polymethoxyflavonoid, nobiletin, is a novel MEK inhibitor that exhibits antitumor metastasis in human fibrosarcoma HT-1080 cells. Biochem Biophys Res Commun 2008;366(1):168–73.

[28] Guney Eskiler G, Deveci AO, Bilir C, Kaleli S. Synergistic effects of nobiletin and sorafenib combination on metastatic prostate cancer cells. Nutr Cancer 2019;71(8):1299–312.

[29] Sousa DP, Pojo M, Pinto AT, Leite V, Serra AT, Cavaco BM. Nobiletin alone or in combination with cisplatin decreases the viability of anaplastic thyroid cancer cell lines. Nutr Cancer 2020;72(2):352–63.

[30] Zeinali M, Abbaspour-Ravasjani S, Ghorbani M, Babazadeh A, Soltanfam T, Santos AC, et al. Nanovehicles for co-delivery of anticancer agents. Drug Discov Today 2020;25(8):1416–30.

[31] Wang J, Wolf RM, Caldwell JW, Kollman PA, DA Case. Development and testing of a general amber force field. J Comput Chem 2004;25(9):1157–74.

[32] Jorgensen WL, Chandrasekhar J, Madura JD, Impey RW, Klein ML. Comparison of simple potential functions for simulating liquid water. J Chem Phys 1983;79(2):926–35.

[33] Abraham MJ, Murtola T, Schulz R, Páll S, Smith JC, Hess B, et al. GROMACS: high performance molecular simulations through multi-level parallelism from laptops to supercomputers. SoftwareX 2015;1:19–25.

[34] Hoover WG. Canonical dynamics: equilibrium phase-space distributions. Phys Rev A 1985;31(3):1695.

[35] Nosé S. A molecular dynamics method for simulations in the canonical ensemble. Mol Phys 1984;52(2):255–68.

[36] Nosé S, Klein M. Constant pressure molecular dynamics for molecular systems. Mol Phys 1983;50(5):1055–76.

[37] Parrinello M, Rahman A. Polymorphic transitions in single crystals: a new molecular dynamics method. J Appl Phys 1981;52(12):7182–90.

[38] Hess B, Bekker H, Berendsen HJ, Fraaije JG. LINCS: a linear constraint solver for molecular simulations. J Comput Chem 1997;18(12):1463–72.

[39] Lei L, Zhang Y, He L, Wu S, Li B, Li Y. Fabrication of nanoemulsion-filled alginate hydrogel to control the digestion behavior of hydrophobic nobiletin. Lwt-food Sci Technol 2017;82:260–7.

[40] Cölfen H, Antonietti M. Mesocrystals and nonclassical crystallization. In: Cölfen H, Antonietti M, editors. Nonclassical crystallization. Hoboken: John Wiley & Sons; 2008. p. 73–101.

[41] Albu MG, Ghica MV, Giurginca M, Trandafir V, Cotrut C. Spectral characteristics and antioxidant properties of tannic acid immobilized on collagen drug-delivery systems. Indian Veterin J 2009;60(7):666–72.

[42] Mahmood U, Shukla YN, Thakur RS. Benzoquinones from Costus speciosus seeds. Phytochemistry 1984;23(8):1725–7.

[43] Jowa L, Witz G, Snyder R, Winkle S, Kalf GF. Synthesis and characterization of deoxyguanosine benzoquinone adducts. J Appl Toxicol 1990;10(1):47–54.

[44] Qiu WZ, Zhong QZ, Du Y, Lv Y, Xu ZK. Enzyme-triggered coatings of tea catechins/chitosan for nanofiltration membranes with high performance. Green Chem 2016;18(23):6205–8.

[45] Barrett DG, Sileika TS, Messersmith PB. Molecular diversity in phenolic and polyphenolic precursors of tannin-inspired nanocoatings. Chem Commun 2014;50(55):7265–8.

[46] Mafy NN, Afrin T, Rahman MM, Mollah MYA, Susan MABH. Effect of temperature perturbation on hydrogen bonding in aqueous solutions of different urea concentrations. RSC Adv 2015;5(73):59263–72.

[47] Rossky PJ. Protein denaturation by urea: slash and bond. Proc. Natl. Acad. Sci. U.S.A. 2008;105(44):16825–6.

[48] Clark JH, Locke CJ, White MS. Medium control in a competitive hydrogen bonding system. Spectrochim Acta A 1994;50(5):891–6.

[49] Lu Y, Zhuk A, Xu L, Liang X, Kharlampieva E, Sukhishvili SA. Tunable pH and temperature response of weak polyelectrolyte brushes: role of hydrogen bonding and monomer hydrophobicity. Soft Matter 2013;9(22):5464–72.

[50] Mahoutforoush A, Asadollahi L, Hamishehkar H, Abbaspour-Ravasjani S, Solouk A, Haghbin Nazarpak M. Targeted delivery of pennyroyal via methotrexate functionalized PEGylated nanostructured lipid carriers into breast cancer cells; A multiple pathways apoptosis activator. Adv Pharm Bull 2023;13(4):747–60.

[51] Kita K, Dittrich C. Drug delivery vehicles with improved encapsulation efficiency: taking advantage of specific drug-carrier interactions. Expert Opin Drug Del 2011;8(3):329–42.

[52] Ke X, Ng VWL, Ono RJ, Chan JMW, Krishnamurthy S, Wang Y, et al. Role of non-covalent and covalent interactions in cargo loading capacity and stability of polymeric micelles. J Controlled Release 2014;193:9–26.

[53] Wang J, Wang BM, Schwendeman SP. Characterization of the initial burst release of a model peptide from poly(d,l-lactide-co-glycolide) microspheres. J Controlled Release 2002;82(2):289–307.

[54] Fredenberg S, Wahlgren M, Reslow M, Axelsson A. The mechanisms of drug release in poly(lactic-co-glycolic acid)-based drug delivery systems-a review. Int J Pharm 2011;415(1–2):34–52.

[55] Hancock BC, Parks M. What is the true solubility advantage for amorphous pharmaceuticals? Pharm Res 2000;17(4):397–404.

[56] Chen YY, Liang JJ, Wang DL, Chen JB, Cao JP, Wang Y, et al. Nobiletin as a chemopreventive natural product against cancer, a comprehensive review. Crit Rev Food Sci Nutr 2023;63(23):6309–29.

[57] Klein G, Vellenga E, Fraaije MW, Kamps WA, de Bont ESJM. The possible role of matrix metalloproteinase (MMP)-2 and MMP-9 in cancer, *e.g.* acute leukemia. Crit Rev Oncol Hemat 2004;50(2):87–100.

[58] Van Wart HE, Birkedal-Hansen H. The cysteine switch: a principle of regulation of metalloproteinase activity with potential applicability to the entire matrix metalloproteinase gene family. Proceed Nat Acad Sci 1990;87(14):5578–82.